Laser-driven quasi-static B-fields for magnetized high-energy-density experiments

C. Vlachos, V. Ospina-Bohórquez, P W Bradford, G. Pérez-Callejo, M. Ehret, P. Guillon, M. Lendrin, X. Vaisseau, B. Albertazzi, E. Soussan, et al.

Laser-driven quasi-static B-fields for magnetized high energy-density experiments

C. Vlachos,[1,2,3,*] V. Ospina-Bohórquez,[1,4,5,6] P. W. Bradford,[1,7] G. Pérez-Callejo,[1,8] M. Ehret,[1,9] P. Guillon,[1] M. Lendrin,[1] X. Vaisseau,[4] B. Albertazzi,[10] E. Soussan,[10] M. Koenig,[10] S. Malko,[11] C. Kaur,[12] M. Gjevre,[12] R. Fedosejevs,[12] M. Bailly-Grandvaux,[13] C. A. Walsh,[14] R. Florido,[15] F. Suzuki-Vidal,[16] C. McGuffey,[17] J. Saret,[13] F. N. Beg,[13] T. Chodukowski,[18] T. Pisarczyk,[18] Z. Rusiniak,[18] J. Dostal,[19] R. Dudzak,[19] A. Calisti,[20] S. Ferri,[20] L. Volpe,[9] N. C. Woolsey,[7] L. Gremillet,[4,6] V. Tikhonchuk,[1,21] and J. J. Santos[1,†]

[1] *Université de Bordeaux-CNRS-CEA, Centre Lasers Intenses et Applications (CELIA), UMR 5107, F-33405 Talence, France*
[2] *Institute of Plasma Physics and Lasers, University Research and Innovation Centre, Hellenic Mediterranean University, 74100 Rethymno, Crete, Greece*
[3] *Department of Electronic Engineering, School of Engineering, Hellenic Mediterranean University, 73133 Chania, Crete, Greece*
[4] *CEA, DAM, DIF, F-91297 Arpajon, France*
[5] *Departamento de Física Fundamental, Universidad de Salamanca, 37008 Salamanca, Spain*
[6] *Université Paris-Saclay, CEA, LMCE, 91690 Bruyères-le-Châtel, France*
[7] *York Plasma Institute, School of Physics, Engineering and Technology, University of York, YO10 5DD, United Kingdom*
[8] *Departamento de Física Teórica, Atómica y Óptica, Universidad de Valladolid, 47011 Valladolid, Spain*
[9] *Centro de Laseres Pulsados, Building M5, Science Park, 37185 Villamayor, Salamanca, Spain*
[10] *LULI - CNRS, CEA, Sorbonne Universités, Ecole Polytechnique, Institut Polytechnique de Paris, F-91120 Palaiseau Cedex, France*
[11] *Princeton Plasma Physics Laboratory, Princeton, New Jersey 08543, USA*
[12] *Department of Electrical and Computer Engineering, University of Alberta, Edmonton, T6G1R1 Alberta, Canada*
[13] *Center for Energy Research, University of California San Diego, La Jolla, CA 92093, United States of America*
[14] *Lawrence Livermore National Laboratory, Livermore, California 94550, USA*
[15] *iUNAT–Departamento de Física, Universidad de Las Palmas de Gran Canaria, 35017 Las Palmas de Gran Canaria, Spain*
[16] *Plasma Physics Group, The Blackett Laboratory, Imperial College London, London, SW7 2AZ, UK*
[17] *General Atomics, San Diego, California 92121, USA.*
[18] *Institute of Plasma Physics and Laser Microfusion, 01-497, Warsaw, Poland*
[19] *Institute of Plasma Physics, Czech Academy of Sciences, 182 00, Prague, Czech Republic*
[20] *Aix Marseille Université, CNRS, PIIM, F-13013 Marseille, France*
[21] *Extreme Light Infrastructure ERIC, ELI-Beamlines Facility, 25241 Dolní Brezany, Czech Republic*

(Dated: February 6, 2024)

We present measurements of magnetic fields generated in laser-driven coil targets irradiated by laser pulses of nanosecond-duration, 1.053 µm wavelength, 500 J energy and $\sim 10^{15}$ W/cm^2 intensity, at the LULI2000 facility. Using two perpendicular probing axes, proton deflectometry is used to characterize the coil current and static charge at different times. Results reveal various deflection features that can be unambiguously linked to a looping quasi-steady current of well understood polarity or to a static charging of the coil surface. Measured currents are broadly consistent with predictions from a laser-driven diode-current source and lumped circuit model, supporting the quasi-steady assessment of the discharges. Peak magnetic fields of ~ 50 T at the center of 500 µm diameter coils, obtained at the moderate laser intensity, open up the use of such laser-driven coil targets at facilities worldwide to study numerous phenomena in magnetized high energy-density plasmas, and its potential applications.

I. INTRODUCTION

The ongoing development of strong external magnetic field (B-field) sources at major laser facilities is pushing the frontiers of magnetized laser-driven High Energy Density (HED) plasma experiments. Indeed, the addition of a controlled external B-field could improve the understanding of a plethora of fundamental processes, where theory and models can be quantitatively compared with data. Many examples are of astrophysical interest, e.g. jet formation [1], growth of magnetohydrodynamic instabilities [2], acceleration of particles in magnetized collisionless shocks [3], turbulent amplification of a B-field [4] and magnetic reconnection [5]. Another major avenue of research is the use of external B-fields in inertial confinement fusion (ICF) experiments, where the seed field is amplified by factors of many hundreds as it is advected with the imploding plasma [6]. Such extreme plasma magnetizations appear as an important tool to increase the yields in fusion plasmas [7–9] through the inhibition of heat losses perpendicularly to the magnetic-field lines of force, the mitigation of hydrodynamic instabilities and the magnetic confinement of D-T ions and thermonuclear α-particles [10–15].

Generating strong seed B-fields in $\sim$cm^3 volumes, as required for a majority of these experiments, is not trivial and often requires bulky electrical components that generate a lot of debris. Such external pulsed power coils

* christos.vlachos@u-bordeaux.fr
† joao.santos@u-bordeaux.fr

[16–18] are also facility-dependent systems that can be cumbersome to implement, thus they are not broadly available in laser facilities. Alternatively, laser-driven coil (LDC) targets are an all-optical platform for delivering external B-fields to laser-plasma experiments (see the pioneering works [19–21] and recent review papers [22–25]). Despite some skepticism surrounding the use of LDCs for magnetizing HED experiments [24], these targets have already been successfully tested in a number of contexts, providing B-fields of $\sim 1\,\mathrm{mm}$ spatial extent, used for the radial collimation of relativistic electron beams in overdense matter [26, 27], the impact on the growth of hydrodynamic instabilities [28], the study of magnetized collisionless shocks [29], magnetized plasma jets [30] and magnetic reconnection environments [5, 31–33]. Potentially, they might also be used in magnetized implosion experiments [34].

An LDC target consists of two plates connected by a coil-shaped wire through which a current can be driven, which in turn induces a B-field. A laser is used to drive hot electrons between these plates, establishing a voltage and circulating coil current. Experiments have been done on a variety of different facilities with different laser parameters (energy, duration and wavelength) and various LDC target designs, reporting B-field amplitudes of a wide range [35–47].

One of the major challenges while developing LDC platforms has been to extract reliable B-field measurements that are consistent across several diagnostics. The number of diagnostics capable of measuring fast-rising and multi-tesla B-fields in an environment filled with plasma and broadband EM radiation is very limited. Electromagnetic probes such as B-dots, optical probes for Faraday rotation measurements and proton deflectometry were the principal diagnostics used in the aforementioned experiments. Some of these diagnostics were developed in tandem with the LDC experimental platform itself; learning how best to employ them, where they can be applied and under what conditions has been an ongoing feature of LDC studies [35, 37, 43, 44].

High-frequency B-dot probes can in principle measure the time evolution of a laser-driven coil B-field, but they are prone to electromagnetic noise and damage from ionizing radiation. Faraday rotation optical probing is based on the birefringent property of paramagnetic crystals and can be used for fairly localized measurements of the B-field at millimetric distances from the coil. Nevertheless, shielding the crystal from the harsh laser-plasma interaction environment (particularly x-rays) is a difficult undertaking.

Proton deflectometry is the third principal diagnostic for measuring B-fields, providing two-dimensional "images" of electric and B-fields-induced structures. When a proton beam passes close to a current-carrying conductor, strong electric and B-fields deflect the protons via the Lorentz force, modifying their trajectories. These protons then propagate through free space and are finally deposited on a stack of radiochromic films (RCF) [48]. Typically, the proton beam is generated with a high-power laser tightly focused to intensities $\sim 10^{19}\,\mathrm{W/cm^2}$ onto thin solid-density targets. The main mechanism responsible for the proton generation is the Target Normal Sheath Acceleration (TNSA) [49]. TNSA-proton beams have a broad energy range. Therefore, measurements using different proton energies in different layers of an RCF stack, linked to the Bragg energy absorption peak, exploit the time-of-flight spread in the beam to produce temporally and spatially resolved measurements of the dynamically evolving electric and magnetic fields. In previous experiments with LDCs, both perpendicular [37, 38] and parallel [43, 44] probing were tested, but simultaneous parallel and perpendicular measurements have only been reported in Ref. [50]. In this paper, we also present two-axis deflectometry measurements (see Fig. 1a); however, these were not taken simultaneously in one shot due to facility limitations.

Our experiment was conducted at the LULI2000 laser facility. Driven by the experience in diagnostic techniques gained over several campaigns on different facilities [23, 26, 35, 37, 43, 50], we have attempted to characterize as clearly as possible the laser irradiation conditions, the energy spectra of the hot electron population issued from the laser interaction with the LDC targets, and the resulting coil discharge current and static charging. Unlike some of our previous studies using ns laser intensities up to $10^{17}\,\mathrm{W/cm^2}$ [23, 37], the presented results are limited to driving intensities of a few $10^{15}\,\mathrm{W/cm^2}$, in line with the majority of ns-pulse laser drivers available worldwide.

Using proton deflectometry across two axes of the target, we unambiguously differentiate between electric and magnetic field effects in the proton deflectograms. For the first time, we quantify the coil B-field directly from measurements of proton beam rotation around the coil axis [51]. Furthermore, by sending the loop current parallel and anti-parallel to the proton probe beam, we observe flipping of the teardrop-shaped proton void, demonstrating that the void can be unequivocally attributed to the current flowing through the coil, of well understood polarity, rather than electrostatic effects [52]. Our results are compared and fairly reproduced by modeling of the LDC as a laser-driven diode connected to an RL circuit, as proposed in [53, 54], which accounts for the impedance of the plasma between the plates. This supports our assessment of a quasi-steady discharge current in the coils.

For practical use in future LDC investigations and/or applications, in the Appendix we provide straightforward analytical relationships that connect features in the experimental proton radiographs of the coil region to a current flowing in the wire, for both parallel and perpendicular probing geometries. These are useful for rapid estimation of the coil current given the rotation angle of the proton beam or the width of the teardrop-shaped void.

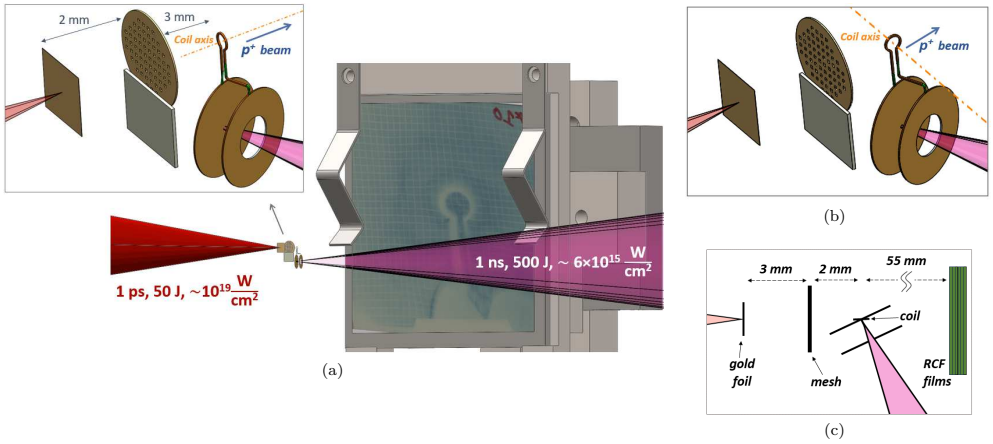

FIG. 1. (1a) Schematic setup for LDC generation of B-field and its characterization by proton deflectometry, at the LULI laser facility. A 1 ns, 500 J, laser pulse of 1.053 µm wavelength is focused to $\sim 6 \times 10^{15}$ W/cm^2 at the target rear plate and gives rise to the coil's B-field. At a controlled delay, a 1 ps, 50 J laser pulse focused to $\sim 10^{19}$ W/cm^2 generates a beam of TNSA protons from a thin foil. This proton source was placed at 5 mm from the LDCs center. Between the Au foil and the coil, we located a mesh to serve as a visual reference in the proton images. A metallic shield was glued at the bottom of the mesh to prevent preheating of the gold foil by the radiation coming from the ns laser interaction region. Protons were detected by a RCF stack placed 55 mm away from the center of the coil, yielding a coil image magnification of 12 at the front RCF layer (corrected for the successive layers). The upper-left inset shows the target region and illustrates the target geometry and the parallel proton probing direction. The holed plate was glued to an insulating stalk in order to mount the target in the chamber. In this configuration, the coil axis crosses the gold foil at the picosecond laser interaction spot and crosses the centers of both the mesh and the RCF stack. (1b) Layout of the target region for proton probing perpendicular to the coil axis, using a slightly different LDCs geometry, in which the coil axis is twisted by 90° compared to the case of parallel proton probing. The proton-probing axis again crosses the coil center. (1c) Top view of the experimental setup (here showing the coil axis perpendicular to the proton-probing axis).

II. EXPERIMENTAL CONFIGURATION

The experiment conducted at the LULI pico 2000 laser facility, where LDC targets were driven by 1.053 µm wavelength (at the fundamental frequency ω_0), $\sim$ 500 J energy, flat-top 1 ns-long ($\sim$ 100 ps rise time) laser pulses. The targets were laser cut from 50 µm thick Cu sheets and assembled in one piece by hand folding. The full target fabrication procedure is of high accuracy and allows for shot to shot reproducibility. They consisted of two parallel disks (3000 µm diameter) connected by a single-turn coil wire (coil radius of 250 µm, with a 50 µm × 50 µm square cross-section). A 1500 µm-diameter hole was placed in the front disk to allow the drive laser access the rear disk. The experimental setup is shown in Fig. 1a, along with an inset showing the LDCs design. The geometry and strength of the driven coil's electric and magnetic fields were probed using proton deflectometry. TNSA proton beams were generated by a short (1 ps FWHM) laser pulse, with 50 J on-target energy, focused up to $\sim 10^{19}$ W/cm^2 intensity onto 10 µm-thick Au foils. Proton energies of more than 20 MeV were measured on successive layers of RCF. The rear surface of the Au foil was located 5 mm away from the coil wire, and TNSA protons were detected by an RCF stack located 55 mm behind the coil resulting in a magnification of 12. The TNSA proton beam direction was either parallel (Fig. 1a) or perpendicular (Fig. 1b) to the coil's symmetry axis to unravel contributions from electric and magnetic fields.

For indirect measurement of the on-target laser intensity and laser-target coupling, we used a time-resolved imaging system looking at the back surface of the irradiated plate, to time the laser-induced shock breakout, and compare it to a hydrodynamic modeling (see Section III A). The inferred laser intensity is compared to an analysis of focal spot images obtained at low energy-flux coupled to on-shot measurements of the laser pulse energy and duration.

To diagnose the temperature of hot electrons generated on the LDC rear plate, we used a Bremsstrahlung cannon spectrometer to record the hard x-ray spectra coming from the interaction region (see Section III B). This cannon consisted of a stack of 15 image plates (IP) with a different filter in front of each plate [55]. The cumulative transmission through each filter is different, allowing multi-channel measurements of x-ray spectra covering 1 keV to 10 MeV. The cannon was placed 51 cm

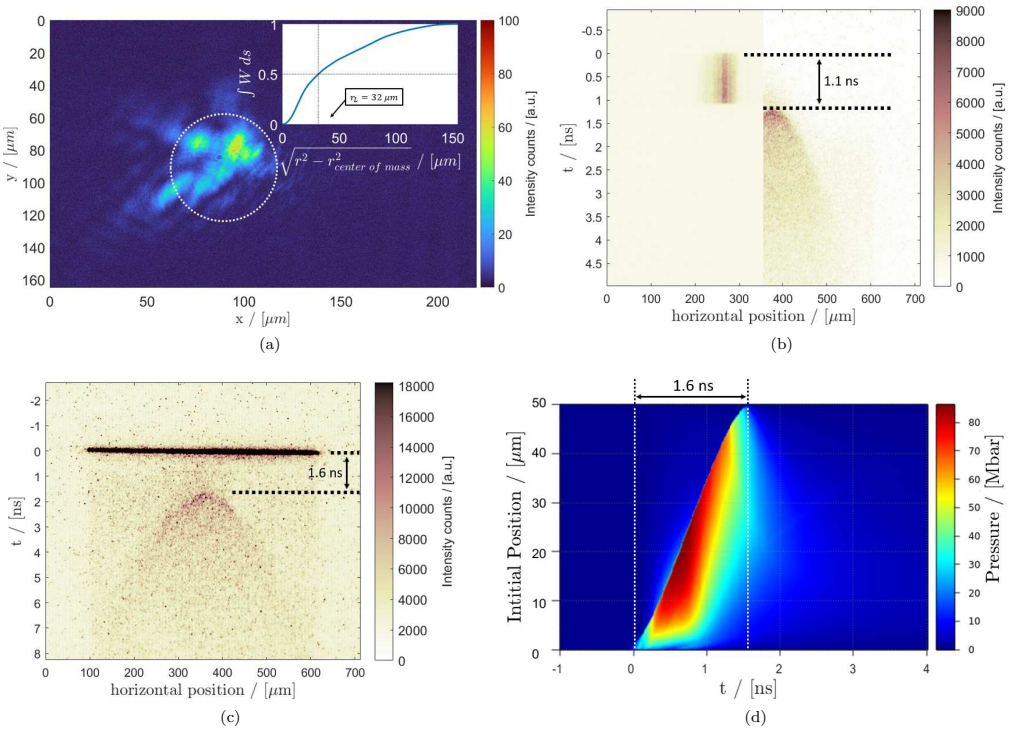

FIG. 2. (2a) A typical image of the nanosecond laser focal spot at low energy flux, obtained on the LULI experiment. The inset graphic shows the integral of the laser energy as a function of the distance from the 2D signal center of mass. Half of the energy is contained inside the dashed circle within a 32 µm radius. (2b) Example of streaked experimental images of the low energy-flux ns laser (left-hand-side) and the shock-breakout self-emission from a full energy shot with a LDCs target (right-hand-side). The measured breakout time was 1.1 ± 0.2 ns. The uncertainty here is mainly due to the jitter of the streak camera trigger when aligning the two signals from the low and high energy flux shots. (2c) Example of an experimental streaked image illustrating the shock breakout self-emission. Here the laser's second harmonic is visible in the same image due to a different filtering, and serves as a time reference of the rising edge of the nanosecond laser, therefore reducing the uncertainty on the measured breakout time to 1.57 ± 0.05 ns. (2d) Example of a MULTI-1D hydrodynamic simulation (pressure) reproducing the experimental shock-breakout time at the rear of a 50 µm Cu layer, for an input laser intensity of 10^{15} W/cm^2 at 1.053 µm wavelength. The ordinate axis represents the initial position of the Cu foil. The abscissa axis is the time, with $t = 0$ corresponding to the beginning of the laser-foil irradiation.

away from target chamber center at an equatorial angle of 27° with respect to the axis of the ns laser drive, facing the front side of the irradiated plate.

III. MEASURING LASER AND PLASMA PARAMETERS

A. Laser Intensity

Our previous experience using LDC targets on different facilities (LULI [37], Gekko [40], Vulcan [50]) suggests that the laser intensity I_L (or irradiance $I_L\lambda^2$, if comparing lasers of different wavelengths) is an important parameter in determining the coil B-field. The laser intensity/irradiance determines the efficiency of the laser energy transfer to hot electrons and the hot electron temperature of the LDCs plasma, which in turn determine the plasma potential, the driven discharge current and ultimately the B-field induced inside the coil.

Two different methods were used to estimate the on-target laser intensity during the experiment. The first method relies on measurements of the laser energy distribution at the focal plane. An imaging system was

Shot	Filter	Breakout time/[ns]
1	OG530	1.1 ± 0.2
2	OG530	1.3 ± 0.2
3	OG580	1.57 ± 0.05
4	OG580	0.90 ± 0.05
5	OG580	1.04 ± 0.05
Average	-	1.2 ± 0.3

TABLE I. Measurements of the shock-breakout time at the rear surface of the 50 µm-thick irradiated plate of the LDCs Cu targets.

directed at the laser focal point, collinear with the axis of the incident laser, and low-flux images of the focused spots were captured by a CCD unit. Due to their irregular shapes, far from a Gaussian distribution (see Fig. 2a), we chose an analysis method that does not include any assumptions about the spatial shape of the beam. First, a background estimation and correction are needed. The post-processing of the images then involved the calculation of the center of mass (counts) of the laser signal. From the energy (counts) distribution of the image as a function of the distance from the center of mass, one can evaluate the radius r_0 which contains 50% of the total energy (see Fig. 2a). Therefore, for a determined r_0, one can calculate an intensity considering the energy and pulse duration on each high-energy shot. This method yielded an average intensity of $(8.1 \pm 4.7) \times 10^{15}\,\mathrm{W/cm^2}$ for $\overline{r_0} = 37\,\mu\mathrm{m}$.

The second independent method for estimating the laser intensity is to measure the shock-breakout time at the rear surface of the laser-driven plate. The same imaging system used to image the laser focal spot was also used to collect optical emission from behind the rear plate of the LDCs onto a streak camera unit, which was synchronized with the ns laser. Figure 2b shows the laser pulse at low energy (without target) on the left-hand side, while the shock-breakout self-emission from a full-energy shot in a LDC target is shown on the right-hand side. For the particular shot shown in Fig. 2b, the measured breakout time was $1.1 \pm 0.2\,\mathrm{ns}$ from the rising edge of the laser pulse. The uncertainty is mainly due to the electronic jitter of the streak trigger signal in between the two independent acquisitions. In some shots, we utilized the OG530 colored glass long-pass filter, while in others, we substituted it with an OG580 filter [56]. This replacement enabled us to observe the laser's second harmonic flash that occurs at the initial stages of its interaction with the target. This effect is depicted in the streak image shown in Figure 2c. The intense horizontal "line" serves here as a jitter-free reference to the laser arrival time, $t = 0$, allowing reducing the uncertainty of the breakout time measurement. In both situations, we apply a Gaussian blur filter to the streaked image ($\sigma = 8$ pixels), which allows us to characterize large variations in brightness and

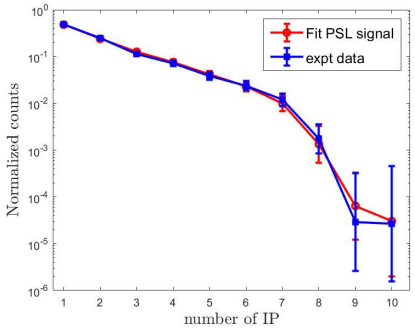

(a)

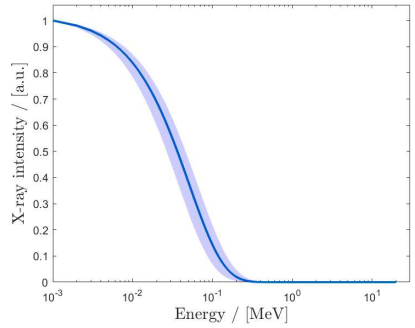

(b)

FIG. 3. (3a) Example analysis of the Bremsstrahlung x-ray spectrum data for one shot. Fit and experimental PSL signals for each IP, normalized to the total number of PSL of the stack. (3b) Normalized synthetic X-ray spectra resulting from the fit of the data.

then using the Canny edge detection algorithm we can accurately define the self-emission region. Finally, we fit a Gaussian function to this region and extract the shock breakout time with respect to $t = 0$. Table I summarizes our different measurements of the shock breakout times.

Once the shock breakout time is known, one can compare it to results from hydrodynamic simulations of shock propagation in the laser-driven foil, where the laser intensity can then be varied until agreement is found between the simulated and experimentally-measured shock transit time. We used the code MULTI-1D, developed by Ramis *et al.* [57]. The post-processing tools used in this work were developed at the LULI laboratory by T. Vinci [58]. In 1D simulations, there is no information about the evolution of the transverse spatial profile of the shock inside the target. Nor is the transverse relaxation occurring at the boundaries of the shocked volume. These

limitations would have been problematic for significantly thicker targets and relatively small laser focal spots. We do not anticipate the 2D phenomena to be important in the case of our experiment, where 50% of the laser energy is focused within a radius which is comparable to the 50 µm target thickness.

A prior comparison of MULTI-1D simulations with other shock breakout measurements at LULI2000 suggests that the laser intensity used in the simulations required to match the data corresponds to $\sim 70\%$ of the actual experimental intensity [58]. A possible reason for this factor could be that in MULTI-1D the drive-laser energy absorption is described uniquely by inverse Bremsstrahlung in the plasma corona up to the critical density, where the laser light is reflected. Accordingly, the values presented in this paper are all corrected by this factor and correspond to the inferred experimental intensity values. Such hydrodynamic analysis leads, for example, to estimate that the on-target laser intensity yielding the shock breakout times of Figs. 2b and 2c was $(4.0^{+4.6}_{-2.0}) \times 10^{15}$ W/cm^2 and $(1.0 \pm 0.2) \times 10^{15}$ W/cm^2, respectively.

Given that the fluctuations in breakout time measured by the streak camera diagnostic during the experiment (see Table I) did not have an impact on the simultaneous measurements of proton-deflectometry, we consider for further analysis the mean of the measured breakout times with an uncertainty that covers the data set: 1.2 ± 0.3 ns. The hydro code reproduces such timing for a laser intensity of $(2.4^{+6.2}_{-1.0}) \times 10^{15}$ W/cm^2.

In summary, the analysis of the low-flux focal spot images suggests a laser intensity of $(8.1 \pm 4.7) \times 10^{15}$ W/cm^2 while the output result from the hydrodynamic simulation analysis suggests an intensity of $(2.4^{+6.2}_{-1.0}) \times 10^{15}$ W/cm^2. The overlapping of the uncertainties from the two different methods yields a working range of laser intensity for the full experiment of $(6.0 \pm 3.0) \times 10^{15}$ W/cm^2, or a laser irradiance of $(6.7 \pm 3.3) \times 10^{15}$ W.cm^{-2}.µm^2.

B. Hot electron temperature

According to existing theoretical models of B-field generation in LDC targets [39, 41, 53], the hot electron temperature T_h in the laser-plasma determines the electron current that can overcome the electrostatic potential between the LDC plates and generate a B-field in the coil. It is therefore important to measure T_h experimentally, because it allows us to test our understanding of LDC operation (see Sec. V).

In our experiment, a Bremsstrahlung cannon spectrometer [55] was used to measure the x-ray spectrum emitted from the laser focus on the LDC rear plate, which allows us to extract information about the energy of the electrons that produced the radiation. The instrument was configured with a stack of 15 image plates (IPs) [59] with a different filter in front of each one, covering a total spectral range from 1 keV to 10 MeV.

The signal on each channel, i.e. each IP, depends on the instrumental response. Consequently, each IP detects radiation emitted in a distinct X-ray spectral range. To unravel the Bremsstrahlung spectrum from the IP signals, we assumed an exponentially decaying spectrum $e^{-\varepsilon_e/T_h}$ which has proved to be adequate in the representation of the Bremsstrahlung emission [55, 59, 60]. We commence with an initial guess for the temperature T_h of the hot electrons, and compute the anticipated Photo-Stimulated Luminescence (PSL) signals for each IP using the equation

$$PSL_i = \Omega_i \int T_i(E) R_{IP}(E) I(E) dE, \qquad (1)$$

where Ω_i is the solid angle subtended by the i-th IP as seen from the target, T_i is the cumulative transmission of the filters and IPs placed in front of the i-th IP [61, 62], R_{IP} is the response function of the IPs, and I is the simulated spectrum.

Subsequently, we employ a least-squares fitting process to compare these simulated signals with the experimental data, enabling us to derive the values of T_h that best reproduce the experimental data.

The Bremsstrahlung data were taken during shots with no proton deflectometry to remove the signal from the relativistic electrons generated by the ps laser. While there were 15 IPs in the Bremsstrahlung cannon, in these shots, only 10 of them measured any signal (this was not the case in the shots with proton deflectometry). We obtained an electron temperature of $T_h \approx 51 \pm 14$ keV, where the uncertainty arises from the fitting procedure and the variation between different shots. Fig. 3a shows an example of the PSL data and the values obtained from the synthetic spectra, while Fig. 3b shows the synthetic bremsstrahlung spectrum together with the corresponding uncertainty region.

IV. MEASURING THE LASER-DRIVEN COIL CURRENT AND CHARGE

A. Proton deflectometry results

Typical proton deflectograms taken from two different shots with either a proton beam probing parallel or perpendicular to the coil axis are shown in Figs. 4 and 5, respectively. The time delay between the arrival of the ns laser driving the LDC target and the ps laser beam that generates TNSA protons was 250 ps in both cases. The proton probing times indicated in each layer of the RCF stacks account for the delay between the lasers and the time-of-flight of the proton energies absorbed on each film, according to the location of the Bragg peak. The delay between the lasers has been varied for other shots.

In parallel probing (Fig. 4), the protons propagating through the coil experience a rotation around the axial B-field (parallel to the proton beam). If there is a metal mesh before the coil target, for spatial reference,

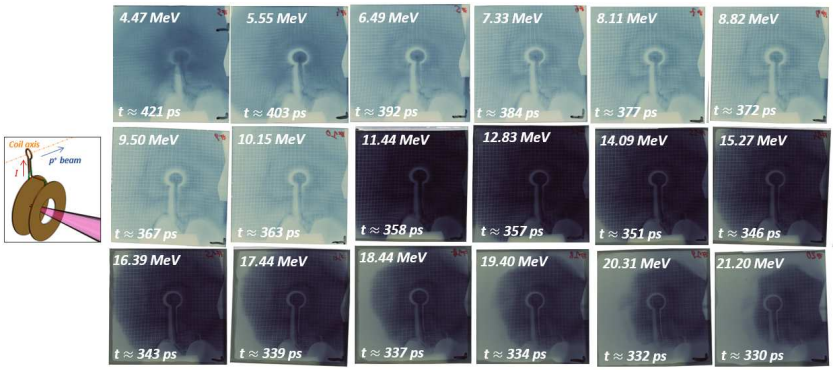

FIG. 4. Scanned experimental RCF images for one shot with parallel proton probing of the laser driven coil (geometry sketched on the left insert), with a lasers' delay set to 250 ps. The perspective is that of the proton beam going into the RCF stack. The front 8 films were HD-V2, while the rear ones were EBT-3 (used for their higher sensitivity). The proton-energy and corresponding probing time labels correspond to the hypothesis that each image mainly corresponds to the Bragg peak deposition of protons of increasing initial kinetic energy.

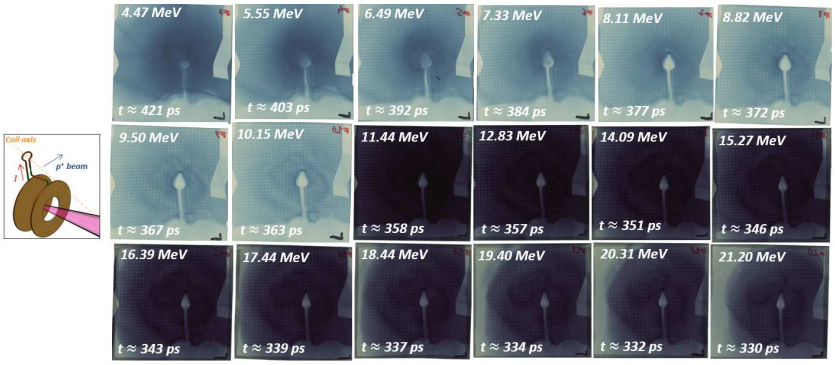

FIG. 5. Same as in Fig. 4 but for one shot with perpendicular proton probing (geometry sketched on the left inset).

one can quantify their rotation with respect to the projected rotation of the mesh image inside the coil. The measured angle of rotation can then be associated with the path-integrated B-field magnitude along the protons' propagation direction. This effect has already been tested in simulations for different scenarios [43] and the mesh rotation does not seem to be significantly affected by electric fields or proton beam divergence. Mesh rotation is, therefore, a reliable metric for measurements of the loop B-field. In this paper, we present experimentally-measured mesh rotation inside an LDC target for the first time.

Another visible feature is the difference in the imprint width of each of the two legs of the coil (see Fig. 4). This can be related to the current flowing through the wire, upwards on the left leg (connected to the irradiated plate) and downwards on the right leg. As the legs are probed by protons which have downwards vertical velocity component, they are defocused and focused by azimuthal fields around the left and right legs respectively. Another possibility for the asymmetry in the leg profiles could be an opposite (static) charge polarity between them, but this scenario seems less plausible because it should lead to a partial shadow/halo rather than a change in imprint width. Wang *et al.* [63] have also used asymmetrical leg profiles in proton deflectograms to quantify the coil B-field.

Finally, "halo" or "sheath"-like structures are consistently observed in our experimental images along the coil and the leg connected to the irradiated plate. They

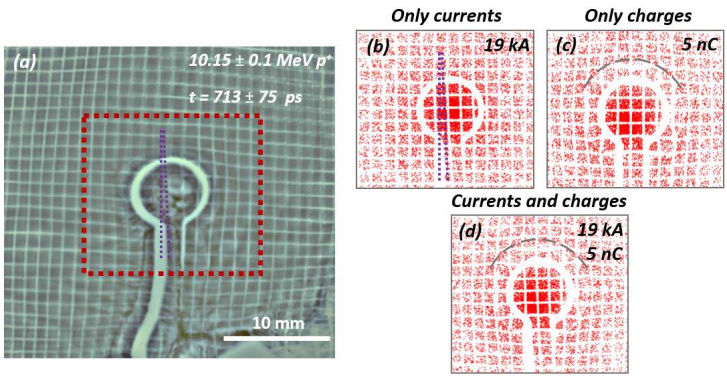

FIG. 6. Parallel proton probing: (a) Zoom into the proton imprint signal on the last HD-V2 layer of the RCF stack. RCF image has been post-processed using a bandpass filter to emphasize the mesh grid lines. The lasers' delay was set to 600 ps. The mesh rotation inside the coil region is estimated to $\sim 3 \pm 0.5°$, as indicated by the angle between the two dashed lines. (b), (c) and (d) Synthetic counterparts of the experimental image for 10.15 MeV protons, assuming respectively, (a) only a coil current (producing the rotation of the mesh imprint), (b) only a torus-distributed static charge (yielding a halo around the coil; identified by the black dashed arc of a circle in the figure), or (c) both coil current and static charge. The values for current and charge are those iteratively found to better match the overall deflection features of the experimental image. Note that for our experimental conditions, unlike in [44], we did not have to assume a non-uniform current path in order to reproduce the main features of the experimental RCF images.

look very regular, following the coil's and wires' geometry. Such features, also present in data from previous experimental campaigns [37, 43], are thought to be the effect of electric fields, since we empirically tested different simulation scenarios and were unable to reproduce this type of "sheath" shape using only B-fields.

The features described above for the parallel proton probing — rotation of the mesh imprint inside the coil, different widths for the legs imprints, and the sheath along the wire – are better visible in Fig. 6a, which is a zoom into a single RCF layer signal.

On the other hand, Fig. 5 shows the signals from an entire stack on a shot in which the coil axis was perpendicular to the proton beam. In this case, the characteristic teardrop-shaped void imprint is clearly visible and corresponds to protons being expelled from the coil region, where fields are concentrated. The top/down asymmetry of the teardrop-shaped void can be understood as the signature of a current looping in the coil according to its polarity (as discussed in Section IV C). The void width is proportional to the coil current, but can also be affected by electric fields around the wire. Indeed, careful scrutiny of Fig. 5 and Fig. 7(a) reveals a double bulb/void feature around the wire: an inner bulb with no proton signal and an outer bulb with a low proton signal. A similar signal with double bulb features was also observed in previous experiments [37, 43, 50]. The outer bulb can be related to the sheath-like structure visible around the coil's legs, which is similar to the one observed in the parallel probing.

In the next section, we show how the halo-structure in the parallel probing and the double-bulb feature in the perpendicular probing can be reproduced by a toroidal charge distribution.

To explain the void and halo structure, we began with the assumption of a positively charged wire surrounded by a concentric ring of negative charge, like in a plasma sheath. Indeed, simulations [64] suggest that concentric annuli of positive and negative charge, centred on the wire, could produce a similar halo with a surrounding caustic. We find, however, that the width and definition of the halo and caustic is highly sensitive to the thickness of each charged layer as well as the location of the current and it was not possible for us to reproduce all aspects of the experimental images with a bipolar sheath-like charge distribution.

Next, we considered spherical and linear static charge distributions, but results did not agree well with the experimental deflectograms. Following Chien *et al.* [46], we also conducted particle tracing simulations with a forward-directed wire current and a return current flowing around the outside, as though through a surrounding plasma, but results were unsuccessful. Finally, a positive toroidal charge distribution and static wire current were able to reproduce the main features of the RCF data in both parallel and perpendicular probing. Although there remains some small uncertainty in the charge polarity/geometry (of a few nC), it is important to note that this does not translate into a significant uncertainty in the coil current, which remains of order of $\gtrsim 10$ kA.

The consistency of parallel and perpendicular simulations with a toroidal charge and uniform wire current

gives us confidence in our ability to identify the different contributions from electric and magnetic fields.

B. Synthetic proton deflectometry analysis

The code 'Particle Field InteractioN' or PAFIN [65] was used to produce the synthetic proton deflectograms presented here. PAFIN is a parallelized 3D simulation code for proton deflectometry and relativistic electron transport through electric and magnetic fields. It can work in a variable 3D environment with various particle sources, detectors, and analytical field set-ups, as well as analytically constant charge and current distributions. PAFIN also contains a field generator for magnetic and electric fields. In our simulations, a monoenergetic, perfectly laminar, divergent beam of protons was propagated through a simulation box containing electrostatic and magnetostatic fields. Simulations were run on a 7 mm-wide, cubic Cartesian grid and upon exiting the grid the protons were transported ballistically to a detector plane located at 51.5 mm as in our experimental configuration. The beam had a Gaussian angular distribution and interactions between individual protons were ignored (a reasonable assumption given the scale of our setup [23]). The energy of the protons used in each simulation was matched to the energy leading to a Bragg peak stopping range at the corresponding RCF layer. A mesh structure (grid) was placed in the path of the proton beam at the same location as in the experiment to obtain information about magnification and spatial scaling in the synthetic detector image. The 42 µm mesh pitch as well as the shadow of the laser-driven coil can be seen clearly in the synthetic deflectograms, e.g. in Figs. 6 and 7. By comparing the synthetic proton deflectograms with the scanned experimental films, it is possible to infer a value for the current along the coil and the level of static charge.

Synthetic deflectograms of protons probing parallel to the coil axis are shown in Figs. 6(b), (c), and (d), in attempts to reproduce the experimental image in Fig. 6(a). The two dashed lines help to identify the unperturbed (outside the coil region) and rotated (inside the coil) mesh imprints, respectively. For this particular shot, the mesh rotation was $\approx 3.0 \pm 0.5°$, which according to the particle-tracing simulation corresponds to a current through the coil of $\sim 19.0 \pm 3.2$ kA, as demonstrated in Fig. 6(b) reproducing the region of interest outlined by the red square in Fig. 6(a). Note that at the same time, the width difference between the legs' imprint is also reproduced. The synthetic deflectogram of Fig. 6(c) does not consider a current and includes only a static charge of 5 nC distributed uniformly over a torus volume of 80 and 265 μm inner and outer radii, respectively, from the coil geometry. This yields a halo feature consistent with the sheath observed experimentally around the coil (a dashed arc is added in the synthetic image to guide the eye). The shape and size of the charged volume was found after a significant number of iterations in order to best reproduce the experimental feature (until we match the dimensions of the experimental and the synthetic halo). Eventually, the synthetic deflectogram in Fig. 6(d) includes both magnetostatic and electrostatic effects. This combination of static fields can reproduce the overall features of the experimental RCF data, that are the mesh rotation inside the coil, the different widths for the left and right leg imprints and the sheath halo around the coil. For our experimental conditions we did not have to assume transient fields or current non-uniformities in order to reproduce the main characteristics of the RCF data.

The same approach was used for the perpendicular proton probing of the coils, yielding the synthetic deflectograms shown in Figs. 7(b), (c) and (d). In Fig. 7(b) no electric fields were included and there was only a constant current flow of 12 kA through the coil. In Fig. 7(c) only electric fields were considered, corresponding to a static positive toroidal charge distribution with the same dimensions as above. The synthetic deflectogram in Fig. 7(d) includes the summed contribution of the magnetic and electric fields and can reproduce the main characteristics (and their dimensions) of the experimental image to a good degree: the double bulb feature, the teardrop shape and the void width. The relative width size between the outer bulb and the inner void is used as a metric to quantify the amplitude of the current and of the charge. It is worth noting that the simulations of perpendicular proton probing confirmed that the teardrop void shape and size depend on deflections due to both electric and magnetic fields, which was not the case for the pointed features in parallel probing. Indeed, a change in the current can affect at the same time the width of both the inner and the outer bulbs. Similarly, a change in the charge of the torus considering a constant current can affect the width of both bulbs.

The comparison between the different RCFs from a single stack (same shot) with their synthetic counterparts yields independent evaluations of the coil current and charge at each corresponding proton probing time. The evolution of those two quantities according to the void width measurements (from images with perpendicular proton probing) are presented in Figs. 8a and 8b, respectively, for two shots with 0.25 ns and 1.0 ns delays between the two laser pulses. The light green symbols in Fig. 8a evidence how the coil's current decreases with time within the interval scanned in each shot. This observation did not conform with our expectations for the shot with the shorter probing time, since while the ns driver laser is still on, one would expect the current flowing through the coil to increase. Similar behavior, however, has also been observed in other experimental campaigns [37, 43, 50] following a similar analysis. On the other hand, one would indeed expect that after 1 ns the coil current should decrease since the laser is off and there is no energy supply anymore. We indeed observe that the current decrease rate is steeper after 1 ns.

A possible contribution to the pointed counter-intuitive effect at 0.25 ns probing time could be the contribution

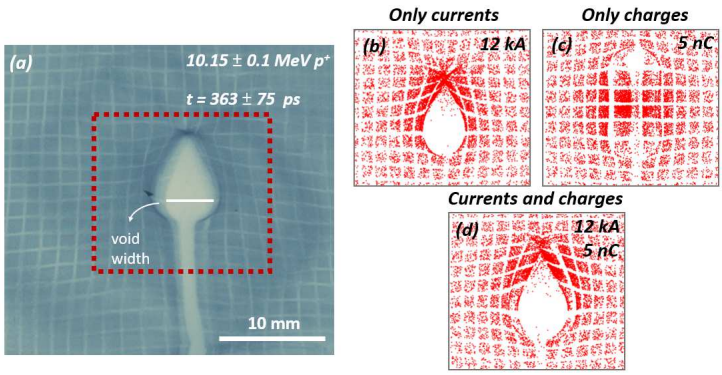

FIG. 7. Same as in Fig. 6 but for perpendicular proton probing of the laser-driven coil. The lasers' delay is 250 ps.

from the most energetic protons depositing part of their energy in previous RCF layers before they stop at a certain film, according to Bragg peak energy deposition. In the experiment, we used 20 RCFs per stack and we observed a strong proton signal even in the 20th film, suggesting a cutoff energy of the proton TNSA beam higher than 21.2 MeV (see Figs. 4 and 5). Hypothetically, if only the higher-energy protons were the main contributors to the imprints observed in the successive RCF layers, one would then expect to extract the same current from every single layer, probed at the same time (delay between lasers plus the proton time of flight) and taking into account only the difference in magnification for the successive layers that can contribute to small differences in bulb width. In order to evaluate such a hypothesis, we assumed a monoenergetic proton beam with a cut-off energy of 25 MeV. The analysis yielded very similar current values for the different RCF layers (variations within the measurement error bars). The average currents inferred from this analysis are represented by the blue squares in Fig. 8a, at the probing times corresponding to the time of flight of 25 MeV protons. While not entirely solving the counter-intuitive current decrease against time for early probing, for further comparison with LDCs modelling (cf. Section V) we simply take the average from all the signals in one stack assuming the Bragg peak absorption.

Another possible contributing factor for the decreasing current trend could also be the decreasing charge over time shown in Fig. 8b. The purple symbols in Fig. 8b show how the coil's charge decreases with time within the interval scanned in each shot. As mentioned earlier in this section, for perpendicular probing the deflections due to the electric and magnetic fields are coupled, and therefore a decreasing charge over time could affect the width of the bulb and therefore the current measurements. Similar to the current analysis shown in Fig. 8a, the blue squares in Fig. 8b correspond to the average inferred charges for proton probing energies of 25 MeV protons.

In shots employing parallel proton probing and considering the precision of our mesh rotation measurements ($\pm 0.5°$), we did not detect any change in the rotation angle within any of the layers (proton energy range $\Delta\varepsilon_p \gtrsim 10$ MeV) in a single stack (same shot). In contrast, PAFIN simulations indicate that a change in the probing proton energy of about 10 MeV corresponds to a rotation angle variation of $1.3 \pm 0.5\,°$. We also did not observe any substantial difference in the amount of charge distributed in the coil region between the different RCF layers ($\lesssim 1$ nC). These observations suggest that assuming the correspondence of different RCF layers with different proton energies within one stack is not valid in this case.

C. Effect of the target geometry

We tested targets of two alternative designs (see Figs. 9a and 9b). Between these two configurations, the current is expected to flow in opposite directions. Therefore, by perpendicular proton probing, one expects the respective imprint void-bulbs to be inverted. Indeed, the corresponding experimental proton imprint images in Figs. 9c and 9d show flipped teardrop-shaped signals. This is a clear indication that the teardrop shape, a characteristic feature of perpendicular proton probing of LDCs, is due to a current flowing through the coil of well-identified polarity, i.e., oriented from the laser-driven plate to the opposite one with the center hole, and not due to some electrostatic effect. To the best of our knowledge, this is the first time that this (rather simple) test has been performed experimentally.

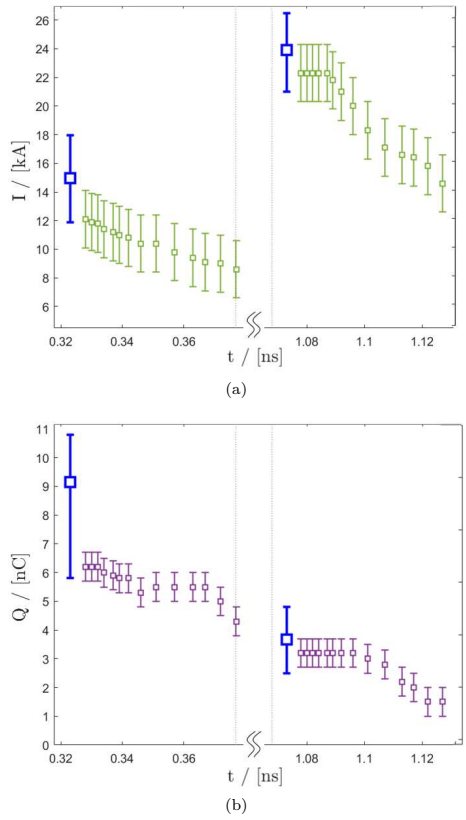

FIG. 8. (8a) Evolution of the coil current evaluated from RCF stacks with perpendicular probing, corresponding to two shots with 0.25 ns and 1 ns delays between the lasers. (8b) Evaluated evolution of the charge corresponding to the same shots as in Fig. 8a. Two distinct extraction analysis are shown: in both plots, the blue squares represent average measurements from all the films in the stack assuming the single proton energy of 25 MeV, capable of crossing all the layers, imprinting them at different depths; while the green (current) and purple (charge) symbols assume that the successive imprints are linked to protons stopped at the absorption Bragg peak of different, increasing initial energy for each successive layer in the RCF stack (and correspondingly decreasing time-of-flight between the Au foil and the coil). Note that the horizontal axes are discontinuous.

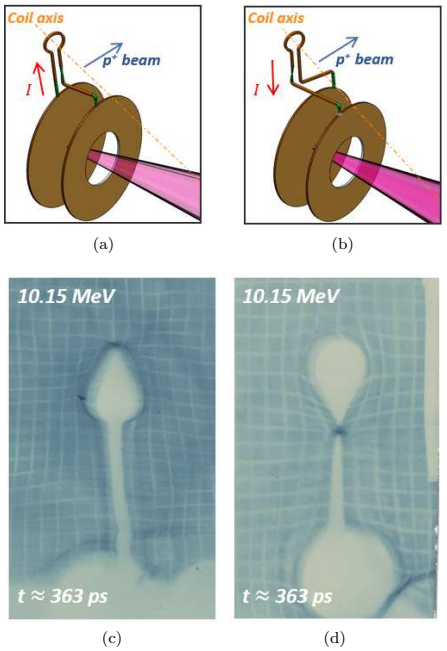

FIG. 9. (9a) "Standard" LDC target design. From the reader's perspective, the current flows clockwise through the coil. (9b) Alternative LDC target design where the current flows anti-clockwise through the coil. (9c)"Standard" teardrop shaped bulb, corresponding to the target shown in (9a). (9d) Radiograph corresponding to target (9b). An inverted bulb-shape is caused by the opposite flow of current in the coil.

V. COIL MODEL BENCHMARKING

Since the first studies were published by Korobkin and Motylev [19] and later by Seely [20] and by Daido *et al.* [21], many different theoretical models have been proposed to explain the physics of B-field generation in LDCs. Some assume that the laser-plasma acts as a current source limited by the expansion time of the inter-plate plasma [21, 39, 41], while others treat it as a voltage source [53, 54, 66]. All treat the plate-coil system as a simple lumped-element circuit to make calculations tractable, though there is also evidence [24] to suggest that the plate-coil system may be too complicated to model in this heuristic manner (particularly if both front and rear plates are simultaneously driven by the laser/x-rays, or if the coil is completely filled with dense plasma). The diode model proposed by Tikhonchuk *et. al* [53] is arguably the most successful in its predictions for the coil current over a wide range of experimental conditions, although a systematic comparison of the various competing models has yet to be published. In this paper, we applied the diode model to our experimental conditions to see if it could reproduce our measurements.

According to the diode model, when a LDC target is irradiated by a nanosecond laser pulse, due to the physical dimensions and the small capacitance of the system, we

can assume that its operation is quasi-stationary. In addition, if we consider that there is a hot electron emission from the laser-heated plate which is able to maintain a potential difference between the plates as long as the laser is on, then we can assume that the system operates as a laser-driven current-source diode.

Considering the system as a RL lumped electric circuit, the evolution of the electric current I is described by the voltage equation:

$$V = L\frac{\mathrm{d}I}{\mathrm{d}t} + \big(Z_d + R\big)I \ , \tag{2}$$

where V is the diode potential and L is the LDC inductance. Williams *et. al* [54] tested the model in a low-intensity laser operation (from 10^9 to $10^{14}\,\mathrm{W/cm^2}$) and concluded that the measured voltage is modified by the plasma between the plates. Accordingly, the resistive part of the circuit ought to account for both the plasma impedance between the plates Z_d (internal impedance) and the resistance of the coil-shaped wire connecting the plates R (making the external circuit). The optimal operation regime is attained when the internal and the external impedances are comparable.

In an attempt, therefore, to explain our measurements from the fitting of the synthetic deflectograms to the experimental RCF data, we applied the laser-driven diode model to the lumped RL-circuit equation, Eq.(2), for the LULI experimental conditions and obtained the time evolution of the current through the coil. As inputs in the model we used the following parameters: laser intensity I_L, laser focal spot radius r_L, hot electron temperature T_h, laser energy conversion efficiency to the hot electron population η_L, coil resistance R, plasma impedance Z_d and coil inductance L. Values for I_L, r_L and T_h have been taken directly from our experimental measurements in Sec. III, while the other parameters were calculated as described below.

Calculating the evolution of current and resistance in the wire is a complex problem [41, 46], but we can use some simple arguments to converge on a representative value of the wire resistance to use in our modelling. The increase rate in temperature T from Ohmic heating can be approximated by $mC_v\frac{\Delta T}{\Delta t} = I^2R$, where C_v is the copper heat capacity and $m = \rho l A$ and $R = \eta_R l/A$ are the wire's mass and resistance, respectively, with l and A denoting the wire's length and cross-section area and ρ and η_R are the copper mass density and resistivity. The area through which the current flows is given by $A \approx 4d\delta$, where d represents the wire thickness and $\delta \sim (\eta_R \Delta t/\mu_0)^{1/2}$ is the skin depth. Substituting A into the heating rate equation yields $\Delta T = \frac{\mu_0 I^2}{16\rho C_v d^2}$, which suggests that the wire temperature is independent of resistivity (within this approximation) but quite sensitive to the wire current.

For a measured current of the order of 10 kA, a wire with $50\,\mu\mathrm{m} \times 50\,\mu\mathrm{m}$ square cross-section and a total length of 5 mm (including coil and legs connected to the plates), the wire will be heated to melting temperature but remain below the temperature of vaporization. Assuming a roughly linear increase in resistivity with temperature (see Eq. (5) in Ref. [46]), the resistance would increase by a factor $\sim 2 - 2.5$ to $R = 0.4 - 0.5\ \Omega$. This is supported by energy conservation, since a current of $10 - 20$ kA will deposit $\sim I^2 R \tau_L \lesssim 0.3$ J in the wire, which is less than the ~ 0.5 J needed to vaporize a wire of mass 0.1 mg. In the following we therefore take $R = 0.4\ \Omega$ as a representative value of the resistance and note that the peak current estimated by the model is only weakly dependent on this value.

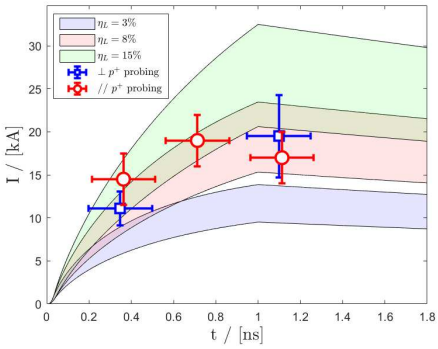

FIG. 10. Evolution of the coil discharge current: Comparison between the diode model predictions and the proton deflectometry measurements. Red circles correspond to currents measured with proton probing parallel to the coil axis, and blue squares to currents measured with proton probing perpendicular to the coil axis. For the model calculations, each colored band corresponds to a different energy conversion efficiency η_L, as labelled, and a hot electron temperature within the interval $T_h = 51 \pm 14$ keV.

The diode impedance for our experimental conditions (according to Refs. [54, 67]) is estimated to be $Z_d \simeq 0.3\sqrt{\mu_0/\epsilon_0}\lambda_{Dh}/r_L \simeq 0.9\,\Omega$, since the hot electron Debye length is $\lambda_{Dh} \simeq 0.4\,\mu$m and the laser spot radius is $r_L \simeq 37\,\mu$m.

Additionally, the LDC inductance L was calculated by computing the magnetic energy W_{mag} of the circuit geometry carrying a current I, according to $W_{\mathrm{mag}} = 0.5LI^2$, in both COMSOL Multiphysics® software [68] and Radia [69], as well as an analytic method [70] in PAFIN and in Matlab [71], which all four agreed within the range $L = 3.7 \pm 0.1$ nH.

Figure 10 shows the comparison between the modeling and the experimental measurements for the LDCs discharge current evolution. Each experimental point represents the average current for one laser shot, estimated from the fitted deflectograms of all the films in the RCF stack, assuming Bragg peak absorption (green symbols in Fig. 8a). The error bars cover the range of values for the entire stack. For the model calculations, we varied the laser energy conversion efficiency to hot electrons η_L,

since it was not a measured parameter in our experiment. In literature, η_L ranges from $\sim 0.1\%$ [72–76] to $\sim 10\%$ [77, 78]. For each value of η_L we considered the lower and upper limits on the range of T_h values according to the uncertainty of the Bremsstrahlung cannon spectrometer measurements. We observed that within the precision of our experiment, we have a conversion efficiency η_L in the range of 3% up to 15%. The best agreement seems to yield $\eta_L \sim 7 - 8\%$.

Figure 11 shows the coil charge evaluated from the experimental data as a function of time (symbols, right-hand-side ordinate axis). Each point is averaged over the full RCF stack from one shot (e.g. average of the purple symbols in Fig. 8b). The evolution of the diode potential is also shown as a red curve (left-hand-side ordinate axis), computed for $T_h = 51\,\text{keV}$ and $\eta_L = 8\%$. Red colored band corresponds to the diode potential with hot electron temperature within the interval $T_h = 51 \pm 14\,\text{keV}$. The charge decreases by roughly only a factor of two over the explored time range. The potential rises very rapidly as hot electrons are ejected from the target, reaching a peak value of $\approx 220 \pm 60\,\text{kV}$ after $\sim 40\,\text{ps}$, and then decreases slowly as the current rises (see Fig. 10), according to the V-I characteristic functions of the diode-source model [53]. According to the predicted maximum voltage and the capacitance of the solid coil wire ($\sim 0.02\,\text{pF}$), we would expect a charge of $\sim 4.4 \pm 1.2\,\text{nC}$. This prediction agrees quite well with the measurements shown in Fig. 11.

The diode-source model for the discharge current in LDC-targets cannot be precisely benchmarked by our measurements because of the uncertainty in the hot electron temperature and the lack of an energy conversion efficiency measurement. Nevertheless, the order of magnitude of the discharge current predicted by the model agrees with our measurements. The measured peak current of 19.5 kA corresponds to a B-field amplitude of 43 T at the center of the coil with a radius of 0.25 mm. The corresponding magnetic energy is $W_{\text{mag}} = 0.7 \pm 0.2\,\text{J}$, corresponding to a conversion efficiency from laser energy of merely $0.14\% \pm 0.05\%$.

It is important to mention that the diode model assumes a relatively low-density column of plasma that bridges the two plates and establishes a potential. It therefore does not account for longer-term effects if the plasma density between the plates is dense and covers a significant internal area. Eventually these effects might short-circuit the coil, as suggested in [21, 24]. Furthermore, plasma inside the coil could alter the B-field geometry and even cause the current to shift from the wire to the plasma itself [44]. Here, however, targets were designed specifically to reduce the plasma ingress into the coil and Fig. 9d clearly shows that the current is confined to the wire, or at least very close to the wire surface. The same can be concluded from all the other RCF images up to our maximum probing time of $t \leq 1.1\,\text{ns}$.

Independently, more experimental work needs to be done in order to benchmark the scalings of both the laser energy conversion efficiency to hot electrons and the temperature of hot electrons with the laser irradiance.

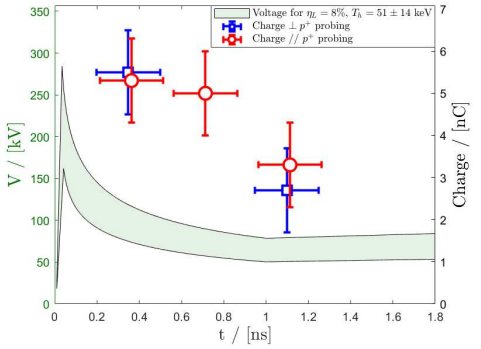

FIG. 11. Evolution of the coil static charge from the experimental measurements (symbols, right-hand-side ordinates) and the diode model prediction of the target potential (curve, left-hand-side ordinates). Red circles and blue squares correspond to measurements with proton probing parallel and perpendicular to the coil axis, respectively. The model calculation assumes $T_h = 51 \pm 14\,\text{keV}$ (inferred from cannon x-ray spectrometer data) and the conversion efficiency of laser energy to hot electrons of $\eta_L = 8\%$.

VI. CONCLUSIONS

In summary, we have presented proton probing of magnetic and electric fields around LDC targets driven by a nanosecond-duration laser at 1 µm wavelength and an intensity of a few $10^{15}\,\text{W/cm}^2$. Proton probing was performed in two directions: perpendicular and parallel to the coil axis, which allowed us to solve the ambiguity between the effects on the probing particles due to static magnetic and electric fields. Particle-tracing simulations reproduce major features in the experimental proton deflectograms under the assumption of a steady current and toroidal volume of positive static charge. The torus of charge is located either around the coil wire or in the interior of the coil, touching the wire's inner surface. Synthetic deflectograms fit the experimental data for both probing directions, in shots with the same probing time, and for different times.

Maximum currents and B-fields of $\sim 20\,\text{kA}$ and ~ 45 T at the centre of 0.5 mm-diameter coils are inferred from multiple different features in the experimental deflectograms, though most reliably from a measured proton beam rotation of $\sim 3°$ in parallel probing. Peak currents and magnetic fields are measured at the end of the driver laser pulse. Inferred currents and B-fields agree well with the predictions of a lumped RL circuit model powered by a laser-driven diode [53], which assumes a quasi-static, uniform current flowing from one plate to another and

through the connecting coil.

While proton deflections due to the B-field are greater in the perpendicular probing geometry – and that is why it has been preferred in most of the setups in the literature – the parallel probing provides an unambiguous measurement of the B-field from the mesh rotation inside the coil shadow, provided the field is strong enough. This said, perpendicular probing is better suited to quantify small B-fields, as in recent tests at the Omega laser facility [34], or for measuring small variations in the B-field strength, such as the case when comparing the various RCF-deflectograms from the same shot.

Parallel proton probing has been used in previous LDC experiments [43, 44, 50], but this paper contains the first quantitative measurements of the coil magnetic field using this technique. By paying careful attention to target design and manufacturing techniques, we have avoided various difficulties alluded to in the literature, such as irregular sheath structures and non-uniform, time-varying coil currents [44]. Our deflectograms show clear evidence of quasi-static currents consistent with the proton void diameter (Fig. 7), void orientation (Fig. 9b), beam rotation, wire shadow and wire halo (Fig. 6) across two orthogonal probing axes.

It is important to highlight some significant factors that contribute towards achieving current uniformity in the target and high-quality measurements of the corresponding magnetic field. Firstly, the target manufacturing process is highly accurate, with each LDC laser-cut from a single Cu sheet and then hand folded into a 3D coil. This ensures good electrical contact between the plates and connecting wire. Secondly, by placing the coil above the drive plate, out of direct line-of-sight of the interaction [79], we reduce plasma ingress into the coil region and x-ray photoionization of the wire [24]. Finally, the ps laser irradiation conditions at LULI2000 are well-controlled, producing high-energy, laminar TNSA proton beams with small source size.

The LDC platform described in this paper is ready for use in application experiments at medium-scale laser facilities. Such platforms allow access to high B-fields over open volumes with minimal excess hardware and debris. Indeed, a B-field of 50 T is enough to strongly magnetize electrons and influence the hydrodynamics of under-dense plasmas generated in laser experiments, of typical densities $\sim 10^{18} - 10^{19}\,\mathrm{cm}^{-3}$ and temperatures from a few 100s eV up to 1 keV – as assessed, respectively, from the Hall parameter $\omega_{ce}/\nu_{ei} \sim 10^2 - 10^3$ (the ratio of the electron cyclotron frequency divided by the mean electron-ion collisional time rate) and from the plasma beta-parameter $\beta = \frac{2\mu_0(n_e T_e + n_i T_i)}{B^2} < 1$ (the ratio between thermal and magnetic pressure). For our coil dimensions of 0.5 mm diameter, the B-field is distributed over a volume of only a few mm^3, but it already provides a new technique for studies of low-beta magnetic reconnection [5] with plasma parameters within the above ranges. For similar plasma density and temperatures, experiments mimicking protostellar jet formation [1] are feasible where the plasma dynamics are modified by the ambient B-field. The extension to time-scales of a few tens of ns, may require the use of longer LDCs laser-pulse drivers [45, 46], and the > 10 mm longitudinal extent of the plasma jets may require the use of multiple coils. In solid-density or even denser plasmas, the higher collision rate makes it more difficult to magnetize the plasma particles. For example, radial confinement of relativistic, MeV-energy scale electron beams in solid-density targets could only be realized using an LDC $\gtrsim 500$ T B-field, which would require a higher laser-intensity drive of $10^{17}\,\mathrm{W/cm}^2$ [26].

Though the LDC platform described here produces consistent B-fields (for fixed laser parameters and target design), there are some aspects of the underlying physics that remain poorly understood. In order to obtain an improved understanding of the LDC platform and to be able to optimize its performance, future experimental and numerical work should focus on the evolution of the plasma characteristics between the LDC target plates. The evolution of the plasma density, self-generated B-field, and residual current transported between the plates is essential for further validation of the diode model, which assumes an equivalence between the plasma and coil currents. More accurate and statistically-robust measurements of laser energy absorption, as well as the spectral and angular distribution of hot electrons, are also needed. This would allow us to produce predictive scaling laws for ns-duration laser pulses at intensities relevant to LDC studies ($\sim 10^{15} - 10^{17}\,\mathrm{W/cm}^2$).

APPENDIX: ANALYTICAL ESTIMATES OF THE COIL B-FIELD

The values of peak current can be estimated by simplified analytical models that agree with our measurements.

Appendix A: Proton probing parallel to the coil axis

In the case of proton probing parallel to the coil axis, one can estimate the angle of rotation experienced by the fraction of the protons that will traverse through the interior coil region, using a simple analytical calculation. The protons undergo cyclotron rotation around the B-field lines. A 2π rotation corresponds to a distance $\lambda_C = v_p 2\pi/\omega_{cp}$, where v_p is the proton velocity and $\omega_{cp} = eB/m_p$ is the proton cyclotron frequency, e is the proton charge and m_p the proton mass. Therefore, for a given looping current I, the rotation angle perpendicular to the B-field axis can be calculated as follows:

$$\theta = \frac{e}{\sqrt{2 m_p \varepsilon_p}} \frac{\mu_0 I}{2a} \int \frac{B(z)}{B_0}\, dz \,, \tag{A1}$$

where ε_p is the proton kinetic energy, $B(z)$ is the B-field along the z axis, $B_0 \approx \mu_0 I/2a$ is the B-field at the center of the coil of radius a and μ_0 is the vacuum permeability. The non-uniformity of the axial B-field

along the proton beam path (z-axis) is accounted for by the characteristic length given by the integral of the normalized B-field over the probing axis, $\int \frac{B(z)}{B_0} dz$. The value of that integral, typically $\sim 2a$, can be more precisely computed numerically by modeling the 3D spatial B-field distribution for a given conductor geometry. For the LULI LDCs design, the integral yields 0.52 mm, which is close to the $2a = 0.5$ mm.

Once the mesh imprint rotation angle is experimentally characterized, one can easily predict the value of the coil's looping current, using the following equation in practical units:

$$I[\mathrm{kA}] = \frac{a}{\int \frac{B}{B_0} dz} \sqrt{\varepsilon_p[\mathrm{MeV}]}\, \theta_{\mathrm{exp}}[^\circ] \;\approx\; \frac{1}{2} \sqrt{\varepsilon_p[\mathrm{MeV}]}\, \theta_{\mathrm{exp}}[^\circ] \,. \tag{A2}$$

Figure 6 shows an example of an experimental image, where 10.15 MeV protons probe the coil region at 713 ps. A mesh rotation of an angle $\sim 3°$ is estimated. According to Eq.(A2), this would correspond to a looping current of ~ 19 kA. The estimated error in the above calculation is $\pm$ 0.5 ° for the measured angle and propagates to the current as ± 3.2 kA, while the contribution from the uncertainty in the proton energy is considered negligible.

The above calculation can provide a simple and fast way of current estimation and, since the beam rotation angle is not significantly affected by electric fields, it can also be considered as a fairly reliable preliminary measurement of the looping current.

Appendix B: Proton probing perpendicular to the coil axis

According to an analytical calculation proposed by Gao *et al.* [38] and developed by Bradford *et al.* [50], one can calculate the width of the void with the following relation:

$$d_{void} = 4\sqrt{MD\Delta z(\mu_B + \mu_E)} \,, \tag{B1}$$

where M is the system magnification, D is the distance between the coil and the RCF detector and Δz is an assumed value for the length of the region of interest. In our experiment Δz can be thought of as the top part of the coil that seems almost straight, seen from the line of sight of the proton beam and approximately equal to the coil radius. In Eq. (B1), $\mu_B = \frac{e\mu_0 I}{2\pi\sqrt{2m_p\varepsilon_p}}$ represents the B-field effect, where I is the current flowing through the conductor. On the other hand, $\mu_E = \frac{e\lambda}{4\pi\epsilon_0\varepsilon_p}$ corresponds to the electric field contribution, where ϵ_0 is the permittivity of free space and λ is the linear charge density.

If we neglect the electric field term, a rough estimate of the on-axis peak coil B-field can be extracted given a measurement of the void width

$$I[\mathrm{kA}] = 45.15 \frac{d_{void}^2}{MD\Delta z} \sqrt{\varepsilon_p[\mathrm{MeV}]} \,. \tag{B2}$$

PAFIN particle-tracing simulations and results from Eq.(B2) for our experimental data are in a good agreement and within the error estimations. For example, Eq.(B2) yields a current of ~ 12 kA for the 10th layer of the shot shown in Fig. 7, which is similar to the PAFIN output.

Equations (B1) and (B2) still hold assuming a static charge distribution that creates specific data features (e.g. the second bulb in perpendicular proton probing).

ACKNOWLEDGEMENTS

This work has been carried out within the framework of the EUROfusion Consortium, funded by the European Union via the Euratom Research and Training Programme (Grant Agreement No. 101052200 — EUROfusion). Views and opinions expressed are however those of the author(s) only and do not necessarily reflect those of the European Union or the European Commission. Neither the European Union nor the European Commission can be held responsible for them. The involved teams have operated within the framework of the Enabling Research Projects: AWP17-ENR-IFE-CEA-02 *Towards a universal Stark-Zeeman code for spectroscopic diagnostics and for integration in transport codes* and AWP21-ENR-IFE.01.CEA *Advancing shock ignition for direct-drive inertial fusion*.

This work has received funding from the European Union's Horizon 2020 research and innovation program under grant agreement no 871124 Laserlab-Europe.

This research was funded, in part, by l'Agence Nationale de la Recherche (ANR), project ANR-22-CE30-0044. For the purpose of open access, the authors have applied a CC-BY public copyright licence to any Author Accepted Manuscript (AAM) version arising from this submission.

This study has also received financial support from the French State in the framework of the Investments for the Future programme IdEx Université de Bordeaux / GPR LIGHT and from the Spanish Ministry of Science and Innovation through Research Grant No. PID2019-108764RB-I00.

This scientific paper has been published as part of the international project called 'PMW', co-financed by the Polish Ministry of Science and Higher Education within the framework of the scientific financial resources for 2021-2022 under the contract no 5205/CELIA/2021/0 (project no CNRS 239915).

C.V. and V.O.-B. acknowledge the support from the LIGHT S&T Graduate Program (PIA3 Investment for the Future Program, ANR-17-EURE-0027).

R.F. and C.K. acknowledge support from the Natural Sciences and Engineering Research Council of Canada (Grant No. RGPIN-2019-05013).

DATA AVAILABILITY

The data that support the findings of this study are available from the corresponding author upon reasonable request.

[1] B. Albertazzi, A. Ciardi, M. Nakatsutsumi, T. Vinci, J. Béard, R. Bonito, J. Billette, M. Borghesi, Z. Burkley, S. N. Chen, *et al.*, Science **346**, 325 (2014).

[2] B. Khiar, G. Revet, A. Ciardi, K. Burdonov, E. Filippov, J. Béard, M. Cerchez, S. N. Chen, T. Gangolf, S. S. Makarov, *et al.*, Phys. Rev. Lett. **123**, 205001 (2019).

[3] D. P. Higginson, P. Korneev, C. Ruyer, R. Riquier, Q. Moreno, J. Béard, S. N. Chen, A. Grassi, M. Grech, L. Gremillet, *et al.*, Commun. Phys. **2**, 60 (2019).

[4] P. Tzeferacos, A. Rigby, A. F. A. Bott, A. R. Bell, R. Bingham, A. Casner, F. Cattaneo, E. M. Churazov, J. Emig, F. Fiuza, *et al.*, Nat. Commun. **9**, 591 (2018).

[5] S. Zhang, A. Chien, L. Gao, H. Ji, E. G. Blackman, R. Follett, D. H. Froula, J. Katz, C. Li, A. Birkel, *et al.*, Nat. Phys. (2023).

[6] M. Hohenberger, P.-Y. Chang, G. Fiksel, J. P. Knauer, R. Betti, F. J. Marshall, D. D. Meyerhofer, F. H. Séguin, and R. D. Petrasso, Phys. Plasmas **19**, 056306 (2012).

[7] P. Y. Chang, G. Fiksel, M. Hohenberger, J. P. Knauer, R. Betti, F. J. Marshall, D. D. Meyerhofer, F. H. Séguin, and R. D. Petrasso, Phys. Rev. Lett. **107**, 035006 (2011).

[8] L. J. Perkins, B. G. Logan, G. B. Zimmerman, and C. J. Werner, Phys. Plasmas **20**, 072708 (2013).

[9] J. D. Moody, B. B. Pollock, H. Sio, D. J. Strozzi, D. D.-M. Ho, C. A. Walsh, G. E. Kemp, B. Lahmann, S. O. Kucheyev, B. Kozioziemski, *et al.*, Phys. Rev. Lett. **129**, 195002 (2022).

[10] T. Sano, T. Inoue, and K. Nishihara, Phys. Rev. Lett. **111**, 205001 (2013).

[11] B. Srinivasan and X.-Z. Tang, Phys. Plasmas **20**, 056307 (2013).

[12] L. J. Perkins, D. D.-M. Ho, B. G. Logan, G. B. Zimmerman, M. A. Rhodes, D. J. Strozzi, D. T. Blackfield, and S. A. Hawkins, Phys. Plasmas **24**, 062708 (2017).

[13] C. Walsh, K. McGlinchey, J. Tong, B. Appelbe, A. Crilly, M. Zhang, and J. Chittenden, Phys. Plasmas **26**, 022701 (2019).

[14] H. Sio, J. D. Moody, D. D. Ho, B. B. Pollock, C. A. Walsh, B. Lahmann, D. J. Strozzi, G. E. Kemp, W. W. Hsing, A. Crilly, *et al.*, Rev. Sci. Instr. **92**, 043543 (2021).

[15] C. A. Walsh, R. Florido, M. Bailly-Grandvaux, F. Suzuki-Vidal, J. P. Chittenden, A. J. Crilly, M. A. Gigosos, R. C. Mancini, G. Pérez-Callejo, C. Vlachos, *et al.*, Plasma Phys. Contr. F. **64**, 025007 (2022).

[16] B. B. Pollock, D. H. Froula, P. F. Davis, J. S. Ross, S. Fulkerson, J. Bower, J. Satariano, D. Price, K. Krushelnick, and S. H. Glenzer, Rev. Sci. Instr. **77**, 114703 (2006).

[17] B. Albertazzi, J. Béard, A. Ciardi, T. Vinci, J. Albrecht, J. Billette, T. Burris-Mog, S. N. Chen, D. Da Silva, S. Dittrich, *et al.*, Rev. Sci. Instr. **84**, 043505 (2013).

[18] O. V. Gotchev, P. Y. Chang, J. P. Knauer, D. D. Meyerhofer, O. Polomarov, J. Frenje, C. K. Li, M. J.-E. Manuel, R. D. Petrasso, J. R. Rygg, *et al.*, Phys. Rev. Lett. **103**, 215004 (2009).

[19] V. V. Korobkin and S. L. Motylev, Sov. Tech. Phys. Lett. **5**, 1135 (1979).

[20] J. F. Seely, Appl. Phys. B **31** (1983).

[21] H. Daido, F. Miki, K. Mima, M. Fujita, K. Sawai, H. Fujita, Y. Kitagawa, S. Nakai, and C. Yamanaka, Phys. Rev. Lett. **56** (1986).

[22] Z. Zhang, B. Zhu, Y. Li, W. Jiang, D. Yuan, H. Wei, G. Liang, F. Wang, G. Zhao, J. Zhong, *et al.*, High Power Laser Sci. Eng. **6** (2018).

[23] J. J. Santos, M. Bailly-Grandvaux, M. Ehret, A. V. Arefiev, D. Batani, F. N. Beg, A. Calisti, S. Ferri, R. Florido, P. Forestier-Colleoni, *et al.*, Phys. Plasmas **25**, 056705 (2018).

[24] J. L. Peebles, J. R. Davies, D. H. Barnak, F. Garcia-Rubio, P. V. Heuer, G. Brent, R. Spielman, and R. Betti, Phys. Plasmas **29**, 080501 (2022).

[25] H. Morita and S. Fujioka, Rev. Mod. Plasma Phys. **7** (2023).

[26] M. Bailly-Grandvaux, J. J. Santos, C. Bellei, P. Forestier-Colleoni, S. Fujioka, L. Giuffrida, J. J. Honrubia, D. Batani, R. Bouillaud, M. Chevrot, *et al.*, Nat. Commun. **9**, 102 (2018).

[27] S. Sakata, S. Lee, H. Morita, T. Johzaki, H. Sawada, Y. Iwasa, K. Matsuo, K. F. F. Law, A. Yao, M. Hata, *et al.*, Nat. Commun. **9** (2018).

[28] K. Matsuo, T. Sano, H. Nagatomo, T. Somekawa, K. F. F. Law, H. Morita, Y. Arikawa, and S. Fujioka, Phys. Rev. Lett. **127**, 165001 (2021).

[29] N. C. Woolsey, Y. A. Ali, R. G. Evans, R. A. D. Grundy, S. J. Pestehe, P. G. Carolan, N. J. Conway, R. O. Dendy, P. Helander, K. G. McClements, *et al.*, Phys. Plasmas **8**, 2439 (2001).

[30] T. Pisarczyk, O. Renner, R. Dudzak, T. Chodukowski, Z. Rusiniak, J. Domanski, J. Badziak, J. Dostal, M. Krupka, S. Singh, *et al.*, Plasma Phys. Contr. F. **64**, 115012 (2022).

[31] X. X. Pei, J. Y. Zhong, Y. Sakawa, Z. Zhang, K. Zhang, H. G. Wei, Y. T. Li, Y. F. Li, B. J. Zhu, T. Sano, *et al.*, Phys. Plasmas **23**, 032125 (2016).

[32] A. Chien, L. Gao, H. Ji, X. Yuan, E. G. Blackman, H. Chen, P. C. Efthimion, G. Fiksel, D. H. Froula, K. W. Hill, *et al.*, Phys. Plasmas **26**, 062113 (2019).

[33] A. Chien, L. Gao, S. Zhang, H. Ji, E. G. Blackman, W. Daughton, A. Stanier, A. Le, F. Guo, R. Follett, *et al.*, Nat. Phys. **19**, 254 (2022).

[34] G. Pérez-Callejo, C. Vlachos, C. A. Walsh, R. Florido, M. Bailly-Grandvaux, X. Vaisseau, F. Suzuki-Vidal, C. McGuffey, F. N. Beg, P. Bradford, *et al.*, Phys. Rev. E **106**, 035206 (2022).

[35] C. Courtois, A. D. Ash, D. M. Chambers, R. A. D. Grundy, and N. C. Woolsey, J. Appl. Phys. **98**, 054913 (2005).

[36] S. Fujioka, Z. Zhang, K. Ishihara, K. Shigemori, Y. Hironaka, T. Johzaki, A. Sunahara, N. Yamamoto, H. Nakashima, T. Watanabe, *et al.*, Sci. Rep. **3**, 1170

(2013).
[37] J. J. Santos, M. Bailly-Grandvaux, L. Giuffrida, P. Forestier-Colleoni, S. Fujioka, Z. Zhang, P. Korneev, R. Bouillaud, S. Dorard, D. Batani, *et al.*, New J. Phys. **17**, 083051 (2015).
[38] L. Gao, H. Ji, G. Fiksel, W. Fox, M. Evans, and N. Alfonso, Phys. Plasmas **23**, 043106 (2016).
[39] G. Fiksel, W. Fox, L. Gao, and H. Ji, Appl. Phys. Lett. **109**, 134103 (2016).
[40] K. F. F. Law, M. Bailly-Grandvaux, A. Morace, S. Sakata, K. Matsuo, S. Kojima, S. Lee, X. Vaisseau, Y. Arikawa, A. Yogo, *et al.*, Appl. Phys. Lett. **108**, 091104 (2016).
[41] C. Goyon, B. B. Pollock, D. P. Turnbull, A. Hazi, L. Divol, W. A. Farmer, D. Haberberger, J. Javedani, A. J. Johnson, A. Kemp, *et al.*, Phys. Rev. E **95**, 033208 (2017).
[42] T. Pisarczyk, J. J. Santos, R. Dudzak, A. Zaras-Szydlowska, M. Ehret, Z. Rusiniak, J. Dostal, T. Chodukowski, O. Renner, S. Gus'kov, *et al.*, J. Instrum. **14** (11), C11024.
[43] P. Bradford, M. Read, M. Ehret, L. Antonelli, M. Khan, N. Booth, K. Glize, D. Carroll, R. Clarke, R. Heathcote, *et al.*, High Power Laser Sci. Eng. **8** (2020).
[44] J. Peebles, J. Davies, D. Barnak, T. Cracium, M. Bonino, and R. Betti, Phys. Plasmas **27**, 063109 (2020).
[45] H. Morita, B. B. Pollock, C. S. Goyon, G. J. Williams, K. F. F. Law, S. Fujioka, and J. D. Moody, Phys. Rev. E **103**, 033201 (2021).
[46] A. Chien, L. Gao, S. Zhang, H. Ji, E. Blackman, H. Chen, G. Fiksel, K. Hill, and P. Nilson, Phys. Plasmas **28**, 052105 (2021).
[47] B. Zhu, Z. Zhang, C. Liu, D. Yuan, W. Jiang, H. Wei, F. Li, Y. Zhang, B. Han, L. Cheng, *et al.*, Matter Radiat. Extrem. **7**, 024402 (2022).
[48] J. F. Dempsey, D. A. Low, S. Mutic, J. Markman, A. S. Kirov, G. H. Nussbaum, and J. F. Williamson, Med. Phys. **27**, 2462 (2000).
[49] S. C. Wilks, A. B. Langdon, T. E. Cowan, M. Roth, M. Singh, S. Hatchett, M. H. Key, D. Pennington, A. MacKinnon, and R. A. Snavely, Phys. Plasmas **8**, 542 (2001).
[50] P. Bradford, A. Dearling, M. Ehret, L. Antonelli, N. Booth, D. C. Carroll, R. J. Clarke, K. Glize, R. Heathcote, M. Khan, J. D. Moody, S. Pikuz, B. B. Pollock, M. P. Read, S. Ryazantsev, C. Spindloe, C. P. Ridgers, J. J. Santos, V. T. Tikhonchuk, and N. C. Woolsey, Plasma Physics and Controlled Fusion **63**, 084008 (2021).
[51] Although parallel proton probing has previously been attempted in several LDC experiments (see Ref. [44, 63, 80]), mesh rotation was either too weak or the proton image too aberrant to extract a quantitative measure of the field.
[52] This deals directly with concerns raised by Peebles *et al.* [24], who stress the difficulty of using perpendicular proton deflectometry to diagnose the LDC B-field.
[53] V. T. Tikhonchuk, M. Bailly-Grandvaux, J. J. Santos, and A. Poyé, Phys. Rev. E **96**, 023202 (2017).
[54] G. Williams, S. Patankar, D. Mariscal, V. Tikhonchuk, J. Bude, C. Carr, C. Goyon, M. Norton, B. Pollock, A. Rubenchik, *et al.*, J. Appl. Phys. **127**, 083302 (2020).
[55] C. D. Chen, J. A. King, M. H. Key, K. U. Akli, F. N. Beg, H. Chen, R. R. Freeman, A. Link, A. J. Mackinnon, A. G. MacPhee, *et al.*, Rev. Sci. Instr. **79**, 10E305 (2008).
[56] For more information on SCHOTT, visit:, `https://www.schott.com/fr-fr/schema-filtre-interactif`.
[57] R. Ramis, R. Schmalz, and J. Meyer-Ter-Vehn, Computer Physics Communications **49**, 475 (1988).
[58] T. Vinci, *Les chocs radiatifs generes par les lasers a haute energie: une opportunite pour l'astrophysique de laboratoire*, Ph.D. thesis, LULI - Laboratoire pour l'utilisation des lasers intenses (2006).
[59] G. Boutoux, D. Batani, F. Burgy, J.-E. Ducret, P. Forestier-Colleoni, S. Hulin, N. Rabhi, A. Duval, L. Lecherbourg, C. Reverdin, *et al.*, Rev. Sci. Instr. **87** (2016), 043108.
[60] Y. Rhee, S. Nam, J. Peebles, H. Sawada, M. Wei, X. Vaisseau, T. Sasaki, L. Giuffrida, S. Hulin, B. Vauzour, *et al.*, Laser Part. Beams **34**, 645–654 (2016).
[61] J. H. Hubbell and S. M. Seltzer, Tables of x-ray mass attenuation coefficients and mass energy-absorption coefficients 1 kev to 20 mev for elements z= 1 to 92 and 48 additional substances of dosimetric interest (1995), available at `https://www.nist.gov/pml/x-ray-mass-attenuation-coefficients`.
[62] X. Vaisseau, *Experimental study of fast electron transport in dense plasmas*, Ph.D. thesis, Universite Bordeaux (2014).
[63] W. Wang, H. Cai, J. Teng, J. Chen, S. He, L. Shan, F. Lu, Y. Wu, B. Zhang, W. Hong, *et al.*, Phys. Plasmas **25**, 083111 (2018).
[64] M. J.-E. Manuel, N. Sinenian, F. H. Séguin, C. K. Li, J. A. Frenje, H. G. Rinderknecht, D. T. Casey, A. B. Zylstra, R. D. Petrasso, and F. N. Beg, Appl. Phys. Lett. **100**, 203505 (2012).
[65] M. Ehret, *Charged particle beam transport in intense electric and magnetic fields*, Master's thesis, Université de Bordeaux and Technische Universtität Darmstadt (2015).
[66] R. Takizawa, H. Morita, K. Matsuo, K. F. F. Law, C. Liu, Y. Arikawa, and S. Fujioka, J. Phys. Soc. Japan **91**, 064501 (2022).
[67] V. T. Tikhonchuk, J. J. Santos, and P. Korneev, Generation of strong magnetic fields with lasers: from nano- to picoseconds, Paper presented at the European Conference On Laser Interaction With Matter, Rethymno, Greece (25 October, 2018).
[68] COMSOL multiphysics® v. 6.1. www.comsol.com. comsol ab, stockholm, sweden.
[69] O. Chubar, P. Elleaume, and J. Chavanne, J. Synchrotron Radiat. **5**, 481 (1998).
[70] R. Dengler, Adv. Electromagn. **5** (2016).
[71] MATLAB, *version 9.10.0 (R2021a)* (The MathWorks Inc., Natick, Massachusetts, 2021).
[72] M. Hohenberger, W. Theobald, S. Hu, K. Anderson, R. Betti, T. Boehly, A. Casner, D. Fratanduono, M. Lafon, D. Meyerhofer, *et al.*, Phys. Plasmas **21**, 022702 (2014).
[73] O. Renner, M. Šmíd, D. Batani, and L. Antonelli, Plasma Physics and Controlled Fusion **58**, 075007 (2016).
[74] G. Cristoforetti, A. Colaïtis, L. Antonelli, S. Atzeni, F. Baffigi, D. Batani, F. Barbato, G. Boutoux, R. Dudzak, P. Koester, *et al.*, Europhys. Lett. **117**, 35001 (2017).
[75] D. Batani, L. Antonelli, F. Barbato, G. Boutoux, A. Colaïtis, J.-L. Feugeas, G. Folpini, D. Mancelli, P. Nicolai, J. Santos, *et al.*, Nucl. Fusion **59**, 032012 (2018).
[76] S. Zhang, C. Krauland, J. Peebles, J. Li, F. Beg, N. Alexander, W. Theobald, R. Betti, D. Haberberger, E. Campbell, *et al.*, Phys. Plasmas **27**, 023111 (2020).
[77] F. Beg, A. Bell, A. Dangor, C. Danson, A. Fews, M. Glinsky, B. Hammel, P. Lee, P. Norreys, and M. Tatarakis,

Phys. Plasmas **4**, 447 (1997).
[78] D. Price, R. More, R. Walling, G. Guethlein, R. Shepherd, R. Stewart, and W. White, Phys. Rev. Lett. **75**, 252 (1995).
[79] M. Ehret, *Charged particle beam acceleration and strong discharge currents' fields generation by laser : a study on laser-driven ion sources and beam transport suited for application in high-energydensity physics experiments.*, Ph.D. thesis, Université de Bordeaux and Technische Universtität Darmstadt (2021).
[80] P. Bradford, N. C. Woolsey, G. G. Scott, G. Liao, H. Liu, Y. Zhang, B. Zhu, C. Armstrong, S. Astbury, and C. e. a. Brenner, High Power Laser Sci. Eng. **6**, e21 (2018).